AIAA JOURNAL
Vol. 34, No. 3, March 1996

Comparison of Planar Fluorescence Measurements and Computational Modeling of Shock-Layer Flow

A. F. P. Houwing*
Australian National University, Canberra 0200, Australia
J. L. Palmer,† M. C. Thurber,† S. D. Wehe,† and R. K. Hanson‡
Stanford University, Stanford, California 94305-3032
and
R. R. Boyce§
University of Queensland, Saint Lucia, Queensland 4072, Australia

Planar laser-induced fluorescence is used to image transient and quasisteady flow phenomena associated with an impulsively started supersonic jet incident on a circular cylinder. The transient phenomena observed are consistent with established theoretical work on the development of nozzle flows in a shock tunnel and with well-understood shock reflection processes. The technique is also used to measure the rotational temperature in the jet and in the shock layer on the cylinder after the establishment of quasisteady flow conditions. The inviscid flow between the bow shock and the edge of the boundary layer and the viscous flow within the boundary layer are modeled numerically using an iterative scheme. Good agreement is achieved between the computational and experimental results for most of the imaged field, except for the region near the shock vertex, where flow nonuniformities near the centerline perturb the shock from the shape expected for a uniform incident flow.

Nomenclature

A = effective spontaneous emission rate for states directly and indirectly populated by laser excitation
B = stimulated absorption coefficient
C_{ab} = calibration constant determined from ratio of fluorescence signals at a known temperature
d = diameter of cylinder
E = laser energy fluence; energy per unit area
F = rotational energy of lower laser-coupled state
$f_{J''}$ = fractional population of lower laser-coupled state
g = spectral overlap between laser and absorption line profiles
J'' = rotational quantum number of lower laser-coupled state
k = Boltzmann constant
M = Mach number
M_i = Mach number estimated from wave angle
$M_{i,\mathrm{cor}}$ = Mach number estimated from wave angle and corrected for image misalignment
N_{pe} = number of photoelectrons produced at photodetector element of two-dimensional array
n_0 = number density of absorbing species
P = pressure
Q = effective electronic quenching rate for states directly and indirectly populated by laser excitation
r_{ab} = ratio of fluorescence signals
S/N = signal-to-noise ratio
T = temperature
V_c = collection volume imaged onto detector element
v'', v' = quantum numbers of lower and upper vibrational states, respectively
x = distance measured parallel to nozzle centerline in flow image
y = distance measured perpendicular to nozzle centerline in flow image
α = angle that wave makes with nozzle exit plane
η = overall collection efficiency of optics and detector
θ = angle streamline makes with flow centerline at nozzle exit plane for source flow
λ = wavelength
ϕ = fluorescence yield

Subscripts

a, b = lower laser-coupled states
i = number identifying wave at nozzle exit
S = conditions in nozzle supply reservoir
1 = initial conditions in shock tube driven section, nozzle, and test section
∞ = conditions in freestream at nozzle exit during quasisteady flow

Introduction

ACCURATE prediction of the various physical and chemical phenomena that accompany the hypervelocity flows associated with the re-entry phase of aerospace flight is extremely important to the design of the next generation of reusable spacecraft. Computational fluid dynamics (CFD) modeling of the flowfields encountered during re-entry is hence of paramount interest. CFD codes, however, must be validated against experimental data before they can be used with confidence in a design environment. In this regard, the visualization of transient and quasisteady flow features and the measurement of rotational and vibrational temperatures and chemical species densities in ground-based testing facilities is very important. Of the various optical techniques developed in recent years, planar laser-induced fluorescence (PLIF) has proved most widely successful in imaging and thermometry over a range of flow conditions and has been applied previously to a shock-layer flow over a sphere.[1]

One of the aims of the work reported here was to image the transient phenomena associated with the nonstationary flow created

---

Presented as Paper 95-0515 at the AIAA 33rd Aerospace Sciences Meeting, Reno, NV, Jan. 9–12, 1995; received Feb. 8, 1995; revision received Nov. 15, 1995; accepted for publication Nov. 17, 1995.

*Senior Lecturer, Aerophysics and Laser-Based Diagnostics Research Laboratory, Department of Physics, Faculty of Science. Member AIAA.

†Graduate Research Assistant, High Temperature Gasdynamics Laboratory, Department of Mechanical Engineering. Student Member AIAA.

‡Professor and Chairman, Department of Mechanical Engineering. Associate Fellow AIAA.

§Research Fellow, Department of Mechanical Engineering. Member AIAA.

when a supersonic jet impinges on a circular cylinder; another was to apply the two-line PLIF method to the measurement of the rotational temperature in the quasisteady bow shock flowfield, to demonstrate the suitability of the technique for the validation of computational methods and physical models. The experiments were undertaken in a small-scale shock tunnel, providing a pilot study that would form the basis for subsequent work in a larger facility.[2]

Fluorescence Imaging and Thermometry

Fluorescence Signal

With the PLIF method, the narrowband output from a pulsed laser light source is normally tuned to a rovibronic transition in a molecular species of interest. Using appropriate optical elements, the output of the laser is spread into a thin rectangular sheet and directed through the flow, exciting a fraction of the molecules in the lower laser-coupled quantum state. The subsequent fluorescence is imaged onto a digital camera, thus producing a map of the fluorescence intensity for a cross section of the field. The intensity of the recorded fluorescence depends on a number of factors, including the optical collection efficiency, rotational and vibrational redistribution rates, collisional quenching rate, radiative lifetime, self-absorption, laser intensity, molecular constants, and the initial level population, which is, in turn, a function of the local values of the species temperature(s) and density. For a weak (nonperturbing) laser pulse, the total number of photoelectrons N_{pe} produced at a photodetector element of a two-dimensional array from a collection volume V_c imaged onto the element is[3–5]

$$N_{\mathrm{pe}} = \eta V_c n_0 f_{J''} B E g \phi \tag{1}$$

where η is the overall efficiency of the collection optics and the detector (photoelectrons produced per photon emitted), $f_{J''}$ is the fractional population of the lower laser-coupled rotational state J'', and E is the energy fluence (energy per unit area) of the laser. Here, ϕ is defined as

$$\phi = A/(A+Q) \tag{2}$$

Temperature Measurements

In the current work, two-line PLIF imaging[6] is employed for temperature measurements. This method involves sequentially exciting transitions with different initial states, so that the local rotational or vibrational temperature may be determined from the ratio of the fluorescence signals. Nitric oxide (NO) was selected as the diagnostic species because of its relatively strong absorption cross section, good fluorescence efficiency, and convenient spectroscopic and collisional properties.[6] Table 1 lists the three NO $A^2\Sigma^+ \leftarrow X^2\Pi(0,0)$ band transitions used in the PLIF experiments, along with their unshifted wavelengths λ and lower level rotational energies F. These transitions were chosen because they are spectrally isolated and originate from rotational levels whose energy difference is sufficiently large to give good temperature sensitivity, while maintaining adequate signal levels with high signal-to-noise ratios.[7]

The ratio of two fluorescence signals from the same volume is given by

$$r_{ab} = \frac{[N_{\mathrm{pe}}]_a}{[N_{\mathrm{pe}}]_b} = \frac{B_a}{B_b}\frac{2J_a''+1}{2J_b''+1}\exp\left\{-\frac{[F(J_a'')-F(J_b'')]}{kT}\right\} \tag{3}$$

where the subscripts a and b identify different lower laser-coupled states within the same vibrational level and the rotational population fractions have been assumed to follow a Boltzmann distribution characterized by a temperature T equal to the translational temperature of the gas. Since the same optical setup is used for each transition and the wavelength ranges concerned are similar, the collection efficiency dependence is removed in taking this ratio. A filter that discriminates against scattered laser light and emission from the laser-excited rovibronic band, while passing emission in the red-shifted (0, 1), (0, 2) bands, etc., eliminates potential problems associated with radiative trapping, since these bands terminate in states without significant population at the temperatures encountered. Furthermore, the effects of rotational energy transfer (RET) and vibrational energy transfer (VET) are removed, as the entire ultra-violet spectrum above ~230 nm is collected. It is also assumed that fluorescence yields cancel in the ratio r_{ab}, because the quenching cross sections[8–13] fluorescence lifetimes[8,11] and fluorescence branching ratios[14,15] for the $A^2\Sigma^+$ ($v' = 0$ and 1) states of NO are insensitive to rotational quantum number. The overlap integrals may be eliminated if shot-to-shot fluctuations in the laser spectral profile are insignificant and the broadening and shift of the absorption line are independent of rotational level, as is the case presently. Provided laser intensities are sufficiently low to avoid saturation effects, the signals can be accurately corrected for temporal and spatial fluctuations in laser intensity, by monitoring the laser sheet profile and pulse energy during the experiment. Hence, the temperature at a particular volume imaged onto an element of the photodetector is given by

$$T = \frac{[F(J_b'')-F(J_a'')]}{k\,\ell n(r_{ab}/C_{ab})} \tag{4}$$

where the spectroscopic terms have been incorporated into a constant C_{ab}.

Consideration of the expected flow temperatures and the energy separation between different lower laser-coupled states indicates that PLIF images produced by $Q_1 + P_{21}(18)$ and $Q_{21} + R_1(6)$ excitation are suitable for thermometry in the freestream, in the lower temperature regions of the shock layer, and in the wake of the body. Images produced by $Q_1 + P_{21}(25)$ and $Q_1 + P_{21}(18)$ excitation are also suitable for thermometry in these regions. The best sensitivity over the entire temperature range is provided by combining images produced by $Q_1 + P_{21}(25)$ and $Q_{21} + R_1(6)$ excitation. In the analysis of the results, temperature maps from all possible combinations of line pairs are presented for comparison.

Table 1 Data for NO $A^2\Sigma^+ \leftarrow X^2\Pi(0,0)$ transitions used in PLIF experiments

Line	λ, nm	F, cm^{-1}
$Q_{21} + R_1(6)$	226.09	80.9
$Q_1 + P_{21}(18)$	225.86	602.3
$Q_1 + P_{21}(25)$	225.43	1128.3

Experimental Facility and Procedure

Shock Tunnel Facility

Previous work[16] has described the details of the reflection type shock tunnel facility used in the current investigation. Figure 1 shows a schematic of this facility and the PLIF imaging system, and Fig. 2 illustrates the details of the flow studied. The length of the driver section of the shock tunnel is 1.5 m, whereas the length of the driven section is 4.5 m. The interior cross section of the driven tube is 76 × 76 mm. A converging–diverging nozzle with a conical exit section was used to generate a supersonic stream that impinged on a circular cylinder whose axis was normal to the flow direction. The diverging section of the nozzle, which was 94 mm in length, had a throat diameter of 17.5 mm and an exit diameter of 30 mm, whereas

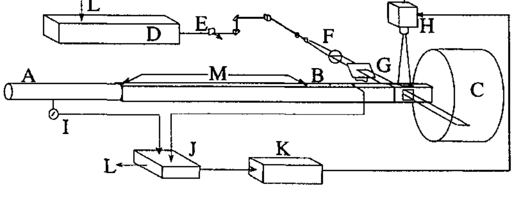

Fig. 1 Schematic of experimental facility with associated optical and electronic components for PLIF imaging: A, driver section; B, driven section; C, dump tank; D, excimer laser, dye laser, and frequency doubler; E, beamsplitter directing fraction of beam to pulse monitor; F, sheet-forming optics; G, beamsplitter directing fraction of beam to laser sheet monitor; H, ICCD camera; I, pressure transducer; J, triggering electronics; K, camera/intensifier control; L, electronic pulse to laser trigger; M, thin-film gauges; and N, data transfer to storage.

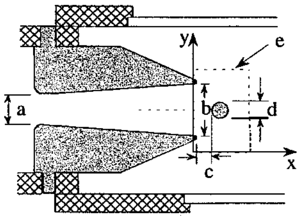

Fig. 2 Schematic showing details of flow geometry and PLIF imaging region; bottom left corner of the imaging region is at $(x, y) = (0, 0)$; top right corner is at (34.4 mm, 51.8 mm); and center of the cylinder is at (17.30 mm, 26.35 mm): a, 17.5 mm; b, 30 mm; c, 8.8 mm; d, 9.5 mm; and e, NO PLIF imaging region 384 × 578 pixels (34.4 × 51.8 mm).

the diameter of the cylinder was 9.5 mm. The cylinder was placed 8.8 mm from the nozzle exit. Ultraviolet grade fused silica windows were mounted in the walls of the test section to provide optical access to the flow under investigation. No diaphragm was used between the nozzle and its supply reservoir. Hence, the conditions in both these regions were identical prior to the operation of the shock tunnel. The filling of the driver gas and the rupture of the shock tube diaphragm were monitored by a pressure transducer located in the wall of the driver section. A number of thin film gauges measured the time of arrival (and hence the average speed) of the primary shock at different locations along the length of the shock tube.

Helium was used for the driver gas, whereas the test gas was a mixture of 0.05% NO in argon (Ar) initially at room temperature and a pressure $P_1 = 8.0$ kPa. Using one-dimensional shock theory and the measured speed of the primary shock wave (1.0 ± 0.01 km/s), one finds that the pressure P_S and the temperature T_S in the nozzle supply reservoir were 440 ± 5 kPa and 2500 ± 30 K, respectively.[16] The nozzle geometry was designed according to one-dimensional isentropic expansion theory to produce a Mach number M_∞ of 3.0 at the nozzle exit, once quasisteady flow had been established. From the imaging results, however, it was found that the flow deviated significantly from ideal one-dimensional behavior. Measurements of the shock stand-off distance in the quasisteady flow and comparisons with CFD predictions of the shock shape (discussed later) indicate that the Mach number was in fact close to 3.5 ± 0.2. This value of M_∞ was thus used to determine the values of the freestream temperature ($T_\infty = 492 \pm 42$ K) and pressure ($P_\infty = 7.5 \pm 1.9$ kPa), by assuming that the expansion was isentropic and one dimensional.

PLIF System

The frequency-doubled output of a pulsed tunable dye laser, using Coumarin 450 dye and pumped with a XeCl excimer laser, was employed to excite transitions at wavelengths of ~226 nm in the $A^2\Sigma^+ \leftarrow X^2\Pi(0,0)$ band of NO. The laser linewidth [full width at half-maximum (FWHM)] was 0.35 ± 0.05 cm^{-1} and the laser energy was approximately 1 mJ per pulse. The optical elements shown in Fig. 1 were used to spread the laser into a thin sheet and to direct it through the flow in the midplane of the nozzle, where it had an approximately Gaussian profile with a FWHM of ~40 mm and a thickness of ~0.4 mm. The fluorescence was imaged with an f/4.5 uv lens onto a cooled intensified camera with a 384 × 578 pixel array, mounted perpendicular to the laser sheet as shown in Fig. 1. A 2-mm UG-5 Schott glass filter, placed in front of the lens, blocked light resonant with the laser as well as visible emission from the test gas. The laser was tuned prior to a series of PLIF experiments by maximizing the fluorescence signal from a low-pressure NO/Ar mixture, monitored with a photomultiplier tube.

The timing sequence required to fire the laser/intensifier/camera system has been described previously by Palmer and Hanson.[17] In the experiments reported here, the time delay that initiated the trigger sequence was varied over a range of values, so that the transient shock phenomena associated with the flow development could be carefully studied. For the thermometry experiments, the delay was chosen so that the flow was quasisteady at the time of measurement, 470 μs after the arrival of the primary shock wave at the entrance of the nozzle.

Data Analysis

The raw data images were corrected for camera background, laser scattering, laser sheet intensity variations, and nonuniform collection efficiency using the methods described by Seitzman et al.[5] and Seitzman and Hanson.[18] The validity of the image correction procedure depends on the assumption that the fluorescence signal is linearly dependent on laser intensity, as was verified experimentally. The image pixels were then binned into superpixels consisting of 2 × 2 original pixels to improve the S/N in the single-shot images and to reduce blurring induced by the motion of the molecules during the fluorescence lifetime,[6] while retaining acceptable spatial resolution. Based on a fluorescence lifetime of ~200 ns and a flow speed of ~1.4 km/s, the maximum motional blur in the freestream is determined to be about 3 pixels or 1.5 superpixels. Negligible blurring occurred in the shock layer.

For the transient flow experiments, $Q_{21} + R_1(6)$ excitation was used, whereas for the quasisteady flow thermometry, all of the transitions listed in Table 1 were used. To further improve the S/N in the case of the quasisteady flow, the signals resulting from excitation of the $Q_{21} + R_1(6)$, $Q_1 + P_{21}(18)$, and $Q_1 + P_{21}(25)$ transitions were averaged over 16, 17, and 10 PLIF images, respectively. The rotational temperature was determined from combinations of these averages, using Eq. (4) and a calibration process to determine the constant C_{ab} in the manner described in earlier work.[5,7]

The inferred temperature field is subject to a number of potential systematic errors that are introduced through errors in the image processing procedure, shot-to-shot fluctuations in the laser spectral profile in both its center frequency and lineshape, the nonlinear dependence of the inferred temperature on the fluorescence signals, and error in the calibration constant C_{ab}. Compared with other contributions, the last two sources are the most important in the current study.

The calibration procedure nearly eliminates the effect of differences in laser tuning and linewidth along the jet axis and in regions of the flow with small radial velocity. Shot-to-shot fluctuations in the laser spectral profile are monitored indirectly by examining the symmetry of the signal about the axis of the jet.[7] If the laser is tuned to the absorption line center (and the laser line shape is symmetric or close to it), the signal will be symmetric about the axis of the jet. Little asymmetry was found to arise from laser attenuation, because the NO concentration was very low. By using only symmetric images for the temperature calculations, one can ensure that the overlap integrals approximately cancel, as the absorption line shape is not a function of rotational level for NO (Ref. 19). Residual effects will be reduced by frame averaging, and the anticipated error is less than ±1% throughout the flowfield.[17]

The nonlinear dependence of the fluorescence signal on temperature may also introduce systematic error into the inferred temperature fields. Uncorrelated random errors in the individual PLIF images, which propagate through the data reduction process, may result in a net positive bias in the average inferred temperature if the sensitivity of the signal ratio to temperature is poor and the S/N of the images is low.[5,6] Because the flow studied here is steady, however, frame and/or spatial averaging may be used to reduce the shot noise in the PLIF signals before the signal ratio is formed and T is inferred. The resulting systematic error is negligible, compared with the remaining random error level in the inferred temperature field. Spatial averaging, applied to the temperature fields to reduce the noise in the final results, introduces additional systematic error only in areas with large temperature gradients, such as across a shock wave. Errors introduced through the determination of C_{ab} depend on the S/N in the calibration region and the uncertainty in the reference temperature. The magnitude of these errors, based on the observed S/N in the images, is assessed in the next section.

CFD Calculations for the Quasisteady Flow

The CFD code used for the calculation of the quasisteady flowfield within the shock layer was developed by Mundt.[20] To economize on the use of computer time, the calculation made in the code is divided into two parts. The first involves the calculation of the inviscid part of the flow (the region between the boundary layer and the shock wave); the second involves the viscous part (the boundary layer on the blunt body). The Euler equations are solved in the inviscid region starting from an initial guess for the shock shape and inviscid flowfield. Second-order boundary-layer equations are solved using a finite difference space-marching method. Both calculations are mathematically simpler and numerically much less intensive than a full Navier–Stokes solution. They are coupled iteratively; the output of one used as the input for the other. Even though the code can take into account chemical nonequilibrium effects, such as dissociation and recombination processes, perfect gas behavior was assumed in the calculations for this investigation.

Results

Transient Flow Features

Figure 3 shows a series of single-shot PLIF images illustrating the transient flow induced when the shock wave expelled from the nozzle collides with the stationary cylinder. Black templates of the cylinder and the outer walls of the nozzle have been superimposed on the images; areas of the flow where solid objects blocked the laser sheet as it traversed the field of view from top to bottom have been masked with white. The signals in these shadow regions are very low, with only small contributions arising from scattered laser light and fluorescence.

A strong fluorescence signal is produced in the stationary room temperature gas surrounding the cylinder, and there is a significant decrease in the signal across the shock as a result of the decrease in Boltzmann fraction with the increase in temperature[16] and the increase in the collisional quenching rate. Hence, the position of the shock wave is easily visualized as the boundary between high and low signals. At the points where the shock wave strikes the cylinder, a reflected shock wave is produced, causing a further increase in temperature and pressure, between the cylinder and the reflected shock and a further decrease in fluorescence intensity. The vortical structures and the expansion fan at the nozzle exit are made visible by the rapid decrease in flow density, which causes a noticeable reduction in fluorescence intensity at their location.

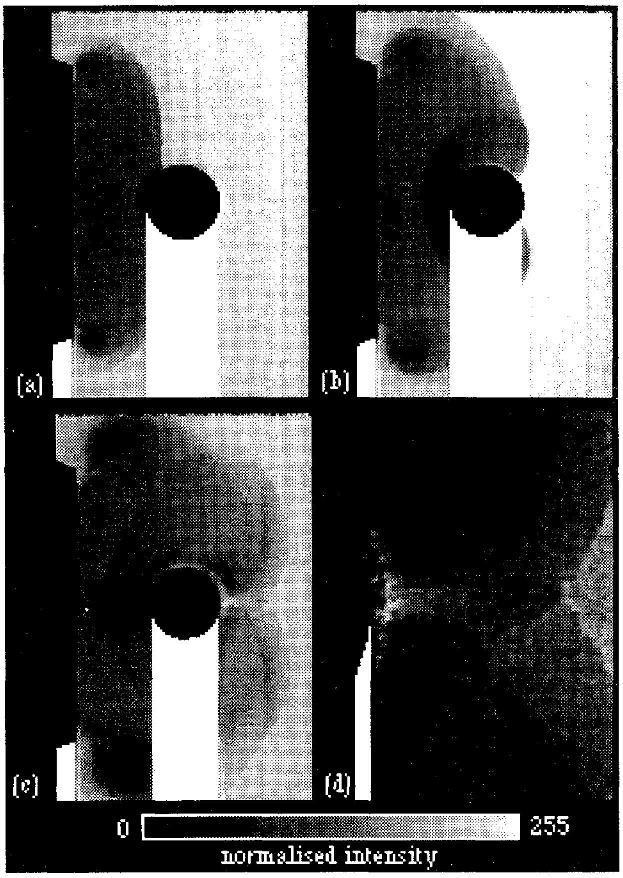

Fig. 3 PLIF images from $Q_{21} + R_1(6)$ excitation showing flow development and transient shock features; delays from time of arrival of primary shock at nozzle entrance; with a-c coordinate system as defined in Fig. 2: a) 97 μs, b) 100 μs, c) 115 μs, and d) 4 times enlargement of c showing Mach reflection behind cylinder.

Figure 3a shows the interaction of the shock wave with the cylinder 97 μs after the arrival of the primary shock at the nozzle entrance. Close examination of the reflection region near the cylinder suggests that the shock wave configuration is one of Mach reflection. The associated Mach stem grows as the expelled shock moves farther downstream. Because the reflecting surface is convex, however, the Mach stem diffracts as it moves along the cylinder. This is clearly evident in Fig. 3b, which shows an image obtained at a delay time of 100 μs. The triple point of the Mach reflection configuration is well resolved, as are all of the major features associated with this type of reflection. In particular, the slipstream can be seen extending from the triple point down to the surface of the cylinder. After the Mach stems on the upper and lower surfaces of the cylinder diffract around the body, they collide, giving rise to another reflected shock configuration. This is clearly observed in Fig. 3c, which shows an image acquired at a delay time of 115 μs. The curved shock to the right of the cylinder is the Mach stem that was initially formed as a result of reflection at the cylinder and has now become the incident shock in this new Mach reflection process. A small Mach stem is evident downstream of the cylinder on the flow centerline in Fig. 3d, which shows an enlarged view of the flow behind the cylinder in Fig. 3c. The resulting reflected shock wave can be seen to intersect the slipstream produced by the previous Mach reflection. Furthermore, the initial stages of the formation of a wake can be seen between the two reflected shock waves directly behind the cylinder.

The interpretation of the shock wave reflection phenomena shown in the PLIF images of Fig. 3 is consistent with the generally understood theory of nonstationary shock wave reflection.[21–25] The existence of vortical structures at the nozzle exit, which are also visible in these images, can be explained by theoretical work on the diffraction of shock waves at the exit of tubes or nozzles.[26–29]

Quasisteady Flow

After a sufficiently long delay, the transient features associated with the nozzle starting process[30] and the reflection process at the cylinder are swept downstream, leaving only the reflected shock to form the bow shock over the cylinder. The position and shape of this bow shock remain constant over a period of ~500 μs, indicating that quasisteady flow has been established. PLIF images of the quasisteady flow are presented in Fig. 4, where single-shot and frame-averaged images from two sets of excitation transitions, $Q_{21} + R_1(6)$ and $Q_1 + P_{21}(18)$, are shown. As already discussed, averaging was performed to improve the S/N and was possible at the quasisteady flow condition because the positions of most of the flow features were constant. Turbulence was evident in the wake flow in the individual PLIF images; however, it was smoothed by the averaging process.

The random error in the PLIF images, primarily resulting from shot noise, was evaluated by examining the statistics of single-shot and frame-averaged signals in various regions of the flow. Results for three regions are presented in Table 2: a region in the freestream about halfway between the nozzle exit and the vertex of the bow shock, a region in the shock layer about halfway between the shock vertex and the stagnation point on the body, and a region close to the stagnation point.

Rotational Temperature Measurements

Figure 5 shows gray-scale contour maps of the rotational temperature fields obtained by applying Eq. (4) to the ratio of fluorescence intensities from different PLIF images. A 0.36 × 0.36 mm area directly in front of the cylinder was chosen as the calibration region for determining the constant C_{ab} because the temperature is equal to the flow stagnation temperature, which for a perfect gas equals that in the nozzle supply reservoir. A region of apparently low temperature directly downstream of the cylinder results from a small misalignment of the cylinder's axis with respect to the optical axis of the imaging system. Because of this misalignment and the cylinder's large aspect ratio, some of the fluorescence originating from the wake region was obstructed.

The propagation of random error in the PLIF signals through various stages of thermometry processing has been discussed previously by McMillin et al.[6] In the current work, the resulting random

Table 2 Shot-noise errors in PLIF images after 2 × 2 binning

		Percentage shot-noise error		
Type of image	Flow region	$Q_{21} + R_1(6)$	$Q_1 + P_{21}(18)$	$Q_1 + P_{21}(25)$
Single	Freestream	7.7	11.7	15.4
Single	Shock layer	11.3	9.6	6.0
Single	Stagnation	30.4	28.7	18.0
Shot average	Freestream	3.1	3.2	4.2
Shot average	Shock layer	2.9	3.5	2.2
Shot average	Stagnation	8.8	9.3	7.2

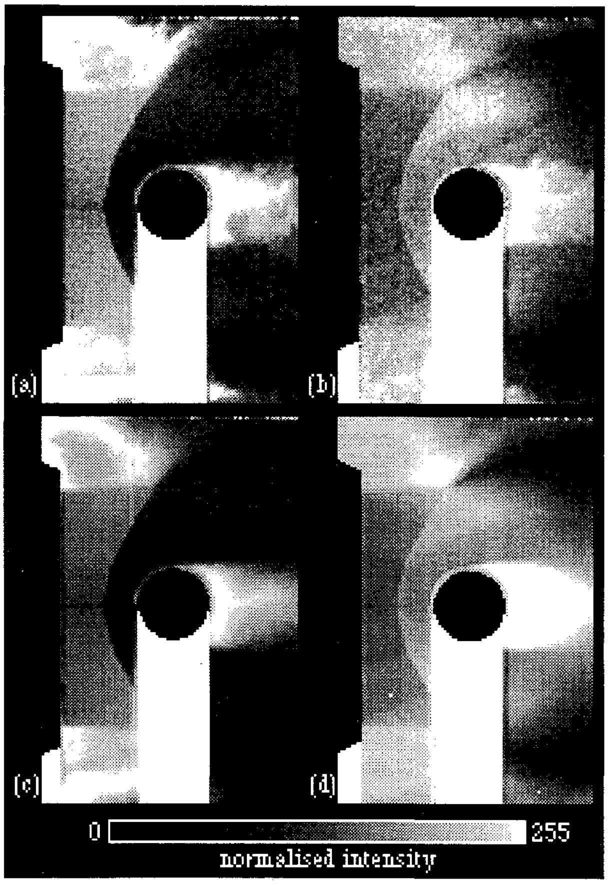

Fig. 4 PLIF images of quasisteady flow over cylinder, coordinate system is as defined in Fig. 2: a) single image from $Q_{21} + R_1(6)$ excitation, b) single image from $Q_1 + P_{21}(18)$ excitation, c) average of 16 images from $Q_{21} + R_1(6)$ excitation, and d) average of 17 images from $Q_1 + P_{21}(18)$ excitation.

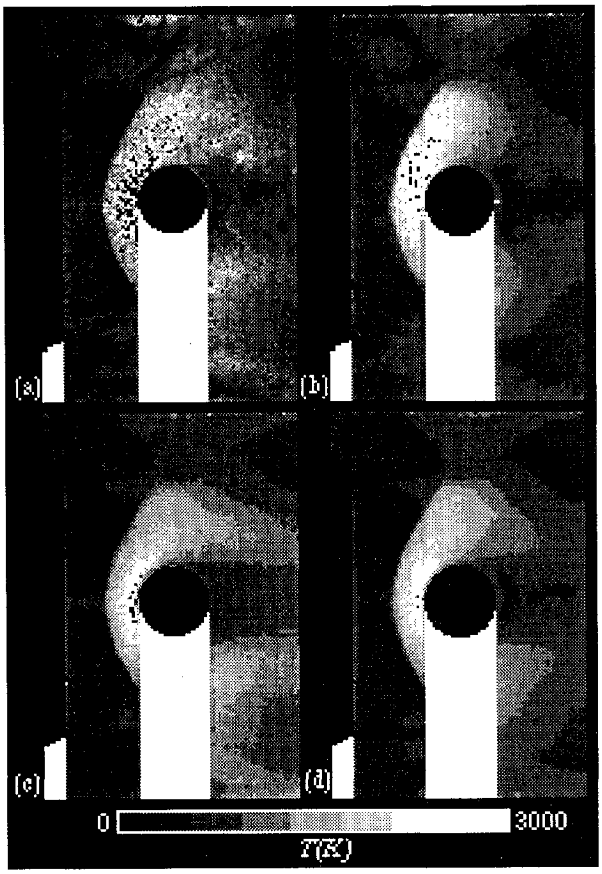

Fig. 5 Temperature maps of quasisteady flow over cylinder, coordinate system is as defined in Fig. 2: maps from a) single $Q_1 + P_{21}(18)$ and $Q_{21} + R_1(6)$ PLIF images, b) averaged $Q_1 + P_{21}(25)$ and $Q_1 + P_{21}(18)$ images, c) averaged $Q_1 + P_{21}(18)$ and $Q_{21} + R_1(6)$ images, and d) averaged $Q_1 + P_{21}(25)$ and $Q_{21} + R_1(6)$ images.

errors in the measured temperatures are smallest for measurements made from the combination of shot-averaged PLIF images with the largest energy difference between the lower laser-coupled states. In particular, for this case, the errors are approximately ±2% in the freestream, ±4% in most of the shock layer, and ±10% near the stagnation point on the cylinder. For temperatures measured from other combinations, these errors are approximately ±4, ±8, and 13%, respectively.

Systematic errors resulting from the nonlinear propagation of uncorrelated (shot-noise) errors are most significant in the shock layer.[31] The largest error of this type occurs for temperature maps obtained from the ratio of single-shot PLIF images with lower laser-coupled states with the smallest energy difference. For these, the error is estimated to be +9%. In all cases, the error is insignificant for temperatures determined from shot-averaged images (less than +1%). The most significant systematic error was that resulting from the uncertainty in the calibration constant C_{ab}. The percentage error in its value is approximately equal to the percentage error in the value of r_{ab} in the stagnation region. The resulting systematic error in the measured temperature can be determined by propagating the uncertainty of C_{ab} through Eq. (4). This error is significant in the shock-layer flow for temperatures determined from single PLIF images (about +14%). For measurements involving shot-averaged data, however, it is reduced to below +2.5% in the shock layer and to less than +0.1% in the freestream.

Figure 5a shows the temperature distribution produced from the combination of a single $Q_1 + P_{21}(18)$ PLIF image and a single $Q_{21} + R_1(6)$ PLIF image. The high level of shot noise in the individual images resulted in a low S/N in the inferred temperature field. Figures 5b–5d display temperature-distribution maps produced by the application of Eq. (4) to shot-averaged PLIF images. Because of this averaging, significantly less noise is present. Figure 6 displays temperature profiles along three vertical cuts for temperature maps derived from single-shot and frame-averaged PLIF images and demonstrates the improvement in S/N that can be achieved through shot averaging. Figure 7 displays a number of temperature profiles to demonstrate the improvement in S/N that can be achieved by convolving the temperature maps with a 0.54 × 0.54 mm averaging function. Ideally this process should be applied to the PLIF images before the application of Eq. (4), although negligible error is introduced here by applying the convolution at this point. By determining the rms noise and mean temperature in a 0.54 × 0.54 mm region on

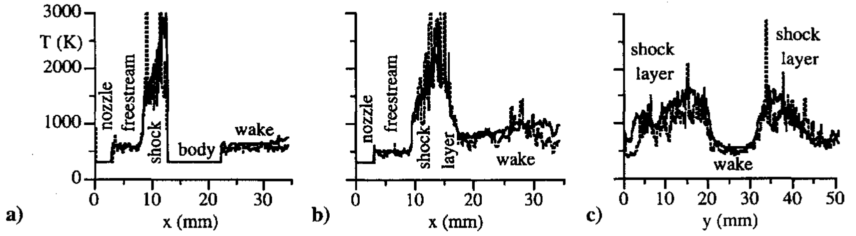

Fig. 6 Temperature profiles in quasisteady flow over cylinder determined from ratio of $Q_1 + P_{21}(18)$ and $Q_{21} + R_1(6)$ PLIF images with xy coordinate system defined in Fig. 2; dashed lines are from ratio of single images, solid lines from ratio of shot-averaged images: a) horizontal cut at $y = 26.35$ mm, b) horizontal cut at $y = 31.55$ mm, and c) vertical cut at $x = 22.94$ mm.

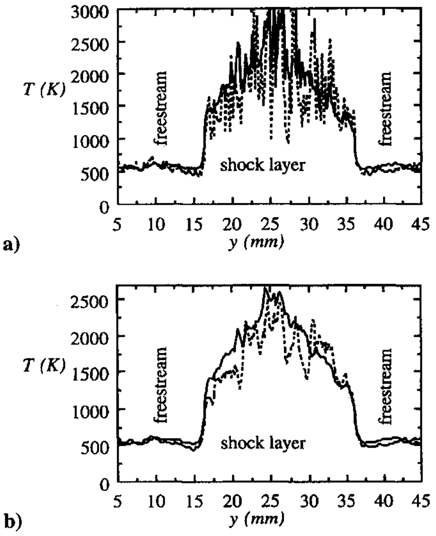

Fig. 7 Measured temperature profiles at $x = 11.65$ mm using $Q_1 + P_{21}(18)$ and $Q_{21} + R_1(6)$ excitation, with xy coordinate system defined in Fig. 2; dashed lines are values of T determined from single PLIF images, solid lines are values determined from shot-averaged PLIF images: a) without additional spatial smoothing and b) with additional spatial smoothing by convolving with a 0.54×0.54 mm rolling average.

the centerline in the shock layer, it is found that for the case of the shot-averaged data, $S/N \approx 10$ before the additional spatial averaging, whereas $S/N \approx 35$ afterwards. This improvement, of course, comes at the expense of a loss in spatial resolution.[5,6]

Freestream Conditions and Flow Uniformity

Although the nozzle was designed for a conical flow with a nominal Mach number of 3, the flow emanating from the nozzle was far from ideal and contained various waves that appeared to originate within the nozzle. Figure 8 presents these waves in a schematic that was obtained by thresholding the shot-averaged PLIF image obtained with $Q_{21} + R_1(6)$ excitation. If one assumes that the flow divergence is very close to a source flow in the region enclosed by the leading characteristics of the expansion waves at the corners of the nozzle, it is possible to estimate the Mach number from the angles of the waves labeled $i = 1$–4 in Fig. 8. The angles α_i that these waves make with the nozzle exit plane are given in Table 3. The assumed source flow is estimated from the nozzle geometry. Hence, at the nozzle exit plane the streamlines are expected to make the angles θ_i with the centerline as given in Table 3. The Mach number M_i at the nozzle exit plane listed in this table has been calculated from the values of θ_i and α_i. The asymmetry in the distribution of α_i is likely caused by a misalignment between the template of the nozzle exit and the true position of the nozzle or by a tilt in the nozzle exit plane with respect to its centerline. If the flow is assumed to be axisymmetric, the distribution is given by the values of $M_{i,\mathrm{cor}}$ listed in the table.

As a result of the nonuniformities in the flow, the Mach number varied throughout the freestream; however, the CFD calculation assumes a uniform Mach number distribution in the jet. To obtain an estimate of an average Mach number M_∞ for the incident flow, the CFD code was run for a range of Mach numbers between 3 and 4, with increments of 0.25, and the predicted shock shape compared with the observed shape, as shown in Fig. 9. The best fit between the experimental and numerical results occurs for $M_\infty = 3.5$. The computed shock shape for $M_\infty = 3.25$ gives reasonably good agreement for the shock standoff distance at the stagnation streamline, but differs markedly with the measured standoff elsewhere. For $M_\infty = 3.5$, the agreement between the computed and observed shock shapes is much better, except close to the stagnation streamline.

The difference between the actual Mach number and the nominal value is the subject of further investigation. One explanation being considered is related to the presence of vortical structures and shocks at the throat of a nozzle with a sharp edged inlet. These features can significantly reduce the effective throat diameter and produce a larger Mach number flow at the nozzle exit.[30] Furthermore, because of the large streamline curvature resulting from the flow circulation at the throat, weak shock waves are established downstream of the

Table 3 Measured wave angles, assumed streamline directions, and calculated Mach numbers at nozzle exit plane

Wave, i	1	2	3	4
α_i, deg	71.3	74.0	77.8	73.5
θ_i, deg	3.8	1.9	1.9	3.8
M_i	2.61	3.25	4.10	2.88
$M_{i,\mathrm{cor}}$	2.74	3.63	3.63	2.74

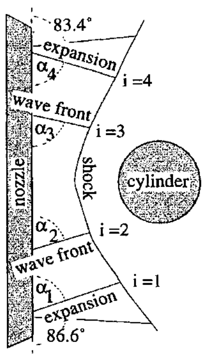

Fig. 8 Schematic showing waves emanating from nozzle and interacting with bow shock on cylinder; figure is to scale, with cylinder diameter d = 9.5 mm.

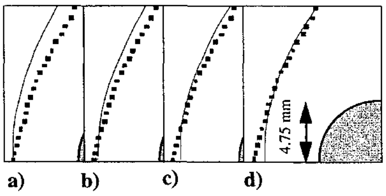

Fig. 9 Computed and experimentally observed shock shapes; plot symbols indicate shock positions measured from PLIF images, solid line gives calculated shock shape for M_∞ = a) 3.0, b) 3.25, c) 3.5, and d) 3.75.

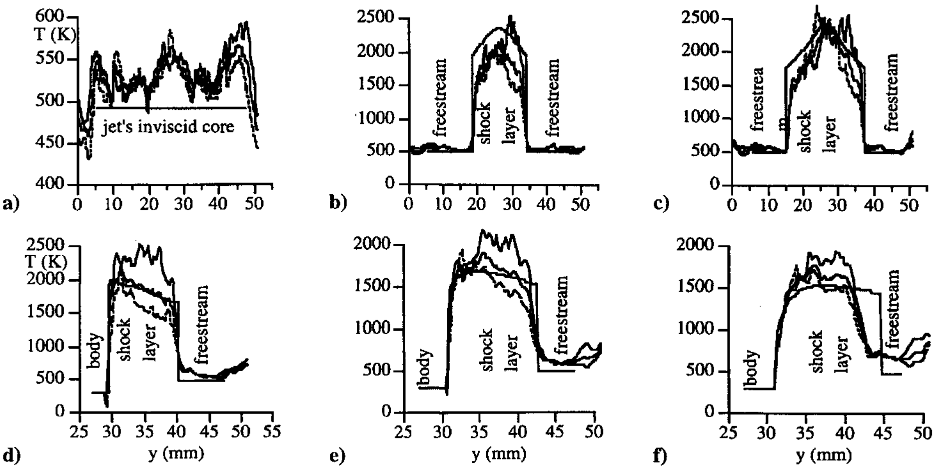

Fig. 10 Computed and measured temperature profiles where the measured temperature has been convolved with a 0.54 × 0.54 mm rolling average and xy coordinate system is defined in Fig. 2; thin line computed, thick line from $[Q_1 + P_{21}(25)]/[Q_1 + P_{21}(18)]$, thin long-dashed line from $[Q_1 + P_{21}(25)]/[Q_{21} + R_1(6)]$, and thin short-dashed line from $[Q_1 + P_{21}(18)]/[Q_{21} + R_1(6)]$; for vertical cuts at: a) $x = 6.81$ mm, b) $x = 10.22$ mm, c) $x = 12.01$ mm, d) $x = 13.80$ mm, e) $x = 15.59$ mm, and f) $x = 17.39$ mm.

Table 4 Comparison of results from different methods of calculating quasisteady conditions

From	M_∞	T_∞, K	P_∞, kPa
Nozzle geometry	3.00	625	13.6
Shock fitting	3.5 ± 0.2	492 ± 42	7.5 ± 1.9
PLIF temperature	3.36 ± 0.06	524 ± 14	8.8 ± 0.7

throat to turn the flow parallel to the nozzle walls. These shock waves weaken further as they extend into the flow and reflect off the walls to produce waves that are observable in the nozzle exit flow. The observation of waves that originate within the nozzle suggests that this occurred; however, further experimental confirmation is required. The nozzle used in the current work was designed with a finite curvature at its inlet, but it is possible that the curvature is still too large to avoid the occurrence of strong vortical structures already described.

CFD and PLIF Comparisons

Figure 10 displays computed and measured temperature profiles in the quasisteady flow along several vertical cuts. Figure 10a shows temperature profiles near the nozzle exit. A temperature spike near the flow centerline is readily apparent. The average flow temperature in the jet was determined from a 3 × 25 mm region in the freestream, midway between the nozzle and bow shock, and found to be 524 ± 14 K. This average temperature can be used to estimate the quasisteady freestream conditions, by assuming an isentropic expansion from the nozzle supply reservoir. Table 4 shows the results of such a calculation compared with the conditions expected from the nozzle geometry and those estimated by the shock-fitting method. Note that, for the calculations based on the shock-fitting method, P_∞ is less than P_1 and the flow is thus predicted to be overexpanded. The shock-fitting method, however, used only a limited number of cases ($M_\infty = 3.00, 3.25, 3.50, 3.75$, and 4.00) and is, hence, expected to produce a less accurate estimate of the quasisteady conditions than that made from the measured freestream temperature. It is therefore expected that the flow is underexpanded.

In Figs. 10b and 10c, the CFD calculation overpredicts the flow temperature in the shock layer by about 15% on the centerline. Larger discrepancies between the numerical and experimental results near the shock front are a consequence of the incorrect prediction of the bow shock's location near its vertex. This observation is consistent with the fact that the CFD code uses uniform conditions in the freestream, whereas, in reality, the flow is nonuniform. In supersonic flows, the flow speed varies inversely with and less rapidly than the temperature. Hence, an increase in freestream temperature on the nozzle centerline produces a decrease in Mach number, yielding a larger shock standoff distance and a smaller temperature ratio across the shock. At positions in the freestream off the flow centerline, one expects significant departures from source flow behavior, so that the component of the Mach number normal to the shock may be significantly different from that expected. In fact, the reduction in temperature observed as one moves away from the centerline is consistent with an expansion that would increase the magnitude of the angle that the streamline makes with the flow centerline, causing a reduction in the Mach number component normal to the shock and a reduction in the temperature ratio across the shock. When coupled with the reduced freestream temperature, this would cause a significant reduction in the postshock temperature, below that predicted by the CFD code.

In Figs. 10c and 10d, good agreement is achieved between the CFD code predictions and the temperature determined from the $[Q_1 + P_{21}(25)]$ to $[Q_{21} + R_1(6)]$ fluorescence ratio. This result, however, is bracketed by the temperature profiles obtained from the $[Q_1 + P_{21}(18)]/[Q_{21} + R_1(6)]$ and $[Q_1 + P_{21}(25)]/[Q_1 + P_{21}(18)]$ fluorescence ratios. The cause of the discrepancy between the three different measurements is not known at this stage and is too large to be a result of systematic errors introduced through random uncertainties in the determination of the constant C_{ab}. In Fig. 10f, significant deviations between the experimental and numerical results can be seen to occur for $y > 40$ mm. The observed reduction in the inferred temperatures below the predicted values is a result of the expansion flow at the shoulder of the nozzle exit intersecting the bow shock on the cylinder.

Conclusions

The PLIF experiments described in this paper allowed the transient flow phenomena associated with the establishment of quasisteady supersonic flow over a circular cylinder at the exit of a shock tunnel nozzle to be clearly visualized. In particular, the images revealed highly resolved cross sections of the flow, rather than projections resulting from integration along the line of sight. The transient phenomena observed were consistent with established theoretical work on the development of shock tunnel nozzle flows and well-understood shock reflection processes.

PLIF thermometry was also successfully applied to the measurement of NO rotational temperatures within the flow surrounding the circular cylinder. The measured temperatures were compared with CFD calculations performed assuming a uniform incident freestream. Good agreement was achieved between the computational and experimental results for most of the imaged field, except for the region near the shock vertex, where flow nonuniformities localized around the centerline perturbed the shock from the shape expected for a uniform incident flow. Clearly, the assumption of a uniform freestream adopted in the CFD calculations was not valid for these flow conditions. To overcome this inadequacy in the modeling it will be necessary first to model correctly the quasisteady flow in the nozzle to determine the distribution of flow parameters (Mach number, temperature, pressure, streamline direction) in the nonuniform jet impinging on the circular cylinder. Second, the CFD code used in this investigation needs to be modified to account for the nonuniformities in the jet. Work to improve the modeling is currently in progress. Improvements to the nozzle design to avoid the presence of perturbing waves in the flow are also being considered.

Acknowledgments

The work was supported by the U.S. Air Force of Scientific Research, Aerospace Sciences Directorate, the Department of Industry, Science, and Technology (Australia), and the Sir Ross and Sir Keith Smith Fund (Australia). The authors gratefully acknowledge the contributions of J. M. Seitzman, D. F. Davidson, and B. K. McMillin to this investigation. The CFD code was used with the kind permission of C. Mundt and E. H. Hirschel.

References

[1] Allen, M. G., Cronin, J. F., Davis, S. J., Foutter, R. R., Parker, T. E., Reinecke, W. G., and Sonnenfroh, D. M., "PLIF Imaging Measurements Compared to Model Calculations in High-Temperature Mach 3 Airflow Over a Sphere," AIAA Paper 93-0092, Jan. 1993.

[2] Houwing, A. F. P., Kamel, M., Morris, C., Thurber, M., Wehe, S., Boyce, R. R., and Hanson, R. K., "PLIF Imaging and Thermometry of NO/N_2 Shock Layer Flows in an Expansion Tube," AIAA Paper 96-0537, Jan. 1996.

[3] Hanson, R. K., Seitzman, J. M., and Paul, P. H., "Planar Laser-Fluorescence Imaging of Combustion Gases," *Applied Physics B*, Vol. 50, No. 6, 1990, pp. 441–454.

[4] Seitzman, J. M., and Hanson, R. K., "A Comparison of Excitation Techniques for Quantitative Fluorescence Imaging of Reacting Flows," *AIAA Journal*, Vol. 31, No. 3, 1993, pp. 513–519.

[5] Seitzman, J. M., Hanson, R. K., and DeBarber, P. A., "Application of Quantitative Two-Line OH Planar Laser-Induced Fluorescence for Temporally Resolved Planar Thermometry in Reacting Flows," *Applied Optics*, Vol. 33, No. 18, 1994, pp. 4000–4012.

[6] McMillin, B. K., Palmer, J. L., and Hanson, R. K., "Temporally Resolved, Two-Line Fluorescence Imaging of NO Temperature in a Transverse Jet in Supersonic Cross Flow," *Applied Optics*, Vol. 32, No. 36, 1993, pp. 7532–7545.

[7] Palmer, J. L., McMillin, B. K., and Hanson, R. K., "Multi-Line Fluorescence Imaging of the Rotational Temperature Field in a Shock-Tunnel Free Jet," *Applied Physics B* (to be published).

[8] McDermid, I. S., and Laudenslager, J. B., "Radiation Lifetimes and Electronic Quenching Rate Constants for Single-Photon-Excited Rotational Levels of NO ($A^2\Sigma^+$, $v' = 0$)," *Journal of Quantitative Spectroscopy and Radiative Transfer*, Vol. 27, No. 5, 1982, pp. 483–492.

[9] Nutt, G. F., Haydon, S. C., and McIntosh, A. I., "Measurement of Electronic Quenching Rates in Nitric Oxide Using Two-Photon Spectroscopy," *Chemical Physics Letters*, Vol. 62, No. 2, 1979, pp. 402–404.

[10] Paul, P. H., Durant, J. L., and Thoman, J. W., "Collisional Quenching Corrections for Laser-Induced Fluorescence Measurements of NO $A^2\Sigma^+$," *AIAA Journal*, Vol. 32, No. 8, 1994, pp. 1670–1675.

[11] Zacharias, H., Halpern, J. P., and Welge, K. H., "Two-Photon Excitation of NO ($A^2\Sigma^+$; $v' = 0, 1, 2$) and Radiation Lifetime and Quenching Measurements," *Chemical Physics Letters*, Vol. 43, No. 1, 1976, pp. 41–44.

[12] Drake, M. C., and Ratcliffe, J. W., "High Temperature Quenching Cross Sections for Nitric Oxide Laser-Induced Fluorescence Measurements," *Journal of Chemical Physics*, Vol. 98, No. 5, 1993, pp. 3850–3865.

[13] Gray, J. A., Paul, P. H., and Durant, J. L., "Electronic Quenching Rates for NO($A^2\Sigma^+$) Measured in a Shock Tube," *Chemical Physics Letters*, Vol. 190, 1992, pp. 266–270.

[14] McGee, T. J., Miller, G. E., Burris, J., and McIlrath, T. J., "Fluorescence Branching Ratios from the $A^2\Sigma^+(v' = 0)$ State of NO," *Journal of Quantitative Spectroscopy and Radiative Transfer*, Vol. 29, No. 4, 1983, pp. 333–338.

[15] McGee, T. J., Miller, G. E., Burris, J., and McIlrath, T. J., "Fluorescence Branching Ratios in Nitric Oxide: Emission from the $A^2\Sigma^+(v' = 1)$ State," *Journal of Quantitative Spectroscopy and Radiative Transfer*, Vol. 34, No. 1, 1983, pp. 81–84.

[16] Palmer, J. L., and Hanson, R. K., "Shock Tunnel Flow Visualization Using Planar Laser-Induced Fluorescence Imaging of NO and OH," *Shock Waves*, Vol. 4, No. 6, 1995, pp. 313–323.

[17] Palmer, J. L., and Hanson, R. K., "Temperature Imaging in a Supersonic Free Jet of Combustion Gases Using Two-Line OH Fluorescence," *Applied Optics* (to be published).

[18] Seitzman, J. M., and Hanson, R. K., "Planar Fluorescence Imaging in Gases," *Instrumentation for Flows with Combustion*, Academic, New York, 1993, pp. 405–466.

[19] Chang, A. Y., DiRosa, M. D., and Hanson, R. K., "Temperature Dependence of Collision Broadening and Shift in the NO *A-X* (0, 0) Band in the Presence of Argon and Nitrogen," *Journal of Quantitative Spectroscopy and Radiative Transfer*, Vol. 47, No. 5, 1992, pp. 375–390.

[20] Mundt, C., "Calculation of Hypersonic Viscous Non-Equilibrium Flows Around Re-Entry Bodies Using a Coupled Boundary Layer Euler Method," AIAA Paper 92-2856, July 1992.

[21] De Rosa, M., Fama, F., and Harith, M. A., "Mach Reflection Phenomenon in the Interaction of Spherical Shock Waves in Air," *Physics Letters A*, Vol. 156, No. 1, 1991, pp. 89–95.

[22] Ben-Dor, G., "Structure of the Contact Discontinuity of Nonstationary Mach Reflections," *AIAA Journal*, Vol. 28, No. 7, 1990, pp. 1314–1316.

[23] Yang, X., Eidelman, S., and Lottati, I., "Shock-Wave Reflection over a Semicircular Cylinder in a Dusty Gas," *AIAA Journal*, Vol. 31, No. 10, 1993, pp. 1737–1743.

[24] Galkowski, A., "Some Remarks on the Theory of Irregular Reflection of a Shock Wave from a Surface," *Archiwum Mechaniki Stos*, Vol. 41, No. 6, 1989, pp. 837–839.

[25] De Rosa, M., Fama, F., and Palleschi, V., "Derivation of the Critical Angle for Mach Reflection for Strong Shock Waves," *Physical Review A15 Statistical Physics Plasmas Fluids*, Vol. 45, No. 8, 1992, pp. 6130–6132.

[26] Bazarov, S. B., Bazhenova, T. V., Bulat, O. V., Golub, V. V., and Shulmeister, A. M., "Three-Dimensional Diffraction of Shock Wave," *Proceedings of the 18th International Symposium on Shock Waves*, edited by K. Takayama, Springer–Verlag, New York, 1992, pp. 251–254.

[27] Abe, A., and Takayama, K., "Shock Wave Diffraction from the Open End of a Shock Tube," *Proceedings of the 17th International Symposium on Shock Waves and Shock Tubes*, edited by Y. W. Kim, American Inst. of Physics, New York, 1990, pp. 270–275.

[28] Matsuo, K., Aoki, T., and Kashimura, H., "Diffraction of a Shock Wave around a Convex Corner," *Proceedings of the 17th International Symposium on Shock Waves and Shock Tubes*, edited by Y. W. Kim, American Inst. of Physics, New York, 1990, pp. 252–257.

[29] Sivier, S., Baum, J., Loth, E., and Lohner, R., "Vorticity Produced by Shock Wave Diffraction," *Proceedings of the 18th International Symposium on Shock Waves*, edited by K. Takayama, Springer–Verlag, New York, 1992, pp. 143–150.

[30] Amman, H. O., and Reichenbach, H., "Unsteady Flow Phenomena in Shock-Tube Nozzles," *Proceedings of the 9th International Symposium on Shock Waves and Shock Tubes*, edited by D. Bershader and W. C. Griffith, Stanford Univ. Press, Stanford, CA, 1973, pp. 96–112.

[31] Seitzman, J. M., and Hanson, R. K., "Two-Line Planar Fluorescence for Temporally Resolved Temperature Imaging in a Reacting Supersonic Flow over a Body," *Applied Physics B*, Vol. 57, No. 6, 1993, pp. 384–391.